

Unsupervised Single Image Super-resolution Under Complex Noise

Zongsheng Yue^{1,3}, Qian Zhao¹, Jianwen Xie², Lei Zhang³, Deyu Meng^{1,*}

¹Xi'an Jiaotong University, Xi'an, China

²Cognitive Computing Lab, Baidu Research, Bellevue, USA

³DAMO Academy, Alibaba Group, Shenzhen, China

{zsyam, timmy.zhaoqian}@gmail.com, jianwen@ucla.edu,
cslzhang@comp.polyu.edu.hk, dymeng@mail.xjtu.edu.cn

Abstract

While the researches on single image super-resolution (SISR), especially equipped with deep neural networks (DNNs), have achieved tremendous successes recently, they still suffer from two major limitations. Firstly, the real image degradation is usually unknown and highly variant from one to another, making it extremely hard to train a single model to handle the general SISR task. Secondly, most of current methods mainly focus on the downsampling process of the degradation, but ignore or underestimate the inevitable noise contamination. For example, the commonly-used independent and identically distributed (i.i.d.) Gaussian noise distribution always largely deviates from the real image noise (e.g., camera sensor noise), which limits their performance in real scenarios. To address these issues, this paper proposes a model-based unsupervised SISR method to deal with the general SISR task with unknown degradations. Instead of the traditional i.i.d. Gaussian noise assumption, a novel patch-based non-i.i.d. noise modeling method is proposed to fit the complex real noise. Besides, a deep generator parameterized by a DNN is used to map the latent variable to the high-resolution image, and the conventional hyper-Laplacian prior is also elaborately embedded into such generator to further constrain the image gradients. Finally, a Monte Carlo EM algorithm is designed to solve our model, which provides a general inference framework to update the image generator both w.r.t. the latent variable and the network parameters. Comprehensive experiments demonstrate that the proposed method can evidently surpass the current state of the art (SotA) method (about 1dB PSNR) not only with a slighter model (0.34M vs. 2.40M) but also faster speed.

1 Introduction

Single image super-resolution (SISR) is an active research topic in computer vision, aiming at recovering the sharp detailed high-resolution (HR) counterpart from a low-resolution (LR) image. As a typical inverse problem, the main difficulties of SISR are mostly attributed to the image degradation, which can be roughly summarized as follows:

- **Unknown of degradation:** In practice, the image degradation is not only unknown but varies with zoom, focus, and camera shake [1] among different LR images.
- **Complexity of degradation:** The degradation is always assumed to be made up of two procedures, i.e., downsampling and noise contamination. Even though the former can be sufficiently approxi-

*Corresponding author.

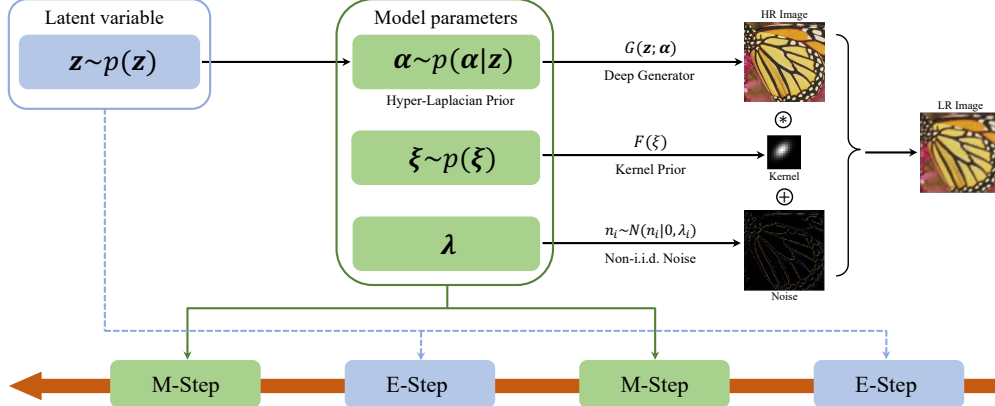


Figure 1: The overview of the proposed SISR method and the elaborately designed EM algorithm. A probabilistic model is constructed to depict the generation process of the observed LR image for the SISR task. It mainly involves in two groups of parameters needed to be inferred, including the model parameters $\{\alpha, \xi, \lambda\}$ and the latent variable z . A Monte Carlo EM algorithm is designed to solve this model, in which the latent variable z and the model parameters $\{\alpha, \xi, \lambda\}$ are alternately updated in the E-Step and M-Step, respectively.

ated by the anisotropic Gaussian kernel followed with a downsampler [2–4], the complex real noise (e.g., camera sensor noise, JPEG compression noise) still makes it very complicated.

Due to such two characteristics of image degradation, the SISR task is extremely challenging.

During the past decades, plenty of SISR methods have been proposed. The earlier interpolation-based methods [5–8] are simple and fast but tend to blur the high frequency details. Afterwards, the model-based unsupervised methods [9–13] are extensively exploited under the maximum a posteriori (MAP) framework. However, such methods rely on manually designed image prior and noise assumptions, which may largely deviate from the true image knowledge. For example, the widely used i.i.d. Gaussian noise assumption is not accordance with the most common camera sensor noise in real world. Different from such model-based SISR methods, the learning-based supervised methods [14–16, 3], especially facilitated by the convolutional neural networks (CNNs), directly learn a mapping from the LR images to the HR ones and achieve significant successes in some ideal scenarios. Nevertheless, their performance depends on the pre-simulated LR/HR image pairs to a great extent, and deteriorates seriously when being applied to real cases with unknown degradation.

Recently, the model-based unsupervised SISR methods are paid attentions again with the advancement of CNNs. The main idea of them is to train a deep super-resolver parameterized by CNN under some elaborately designed prior knowledges, such as the internal recurrence of patches across scales in a single image [1, 17], deep image prior (DIP) [18], deep generative prior (DGP) [19] and so on. Furthermore, DoubleDIP [20, 21] or FKPDIP [4] both extend DIP to the blind SISR task by fitting the blur kernel using a multilayer perceptron (MLP) or normalizing flow [22, 23]. Comparing with the learning-based supervised methods, these methods are with better generalization capabilities when dealing with unknown degradations, mainly because they do not rely on external manually pre-simulated training data. However, such methods also follow the simple i.i.d. Gaussian noise assumption, which hinders their performance in complicated degradations led by complex real noise.

Against these issues, this paper proposes a model-based unsupervised SISR method with a more rational noise assumption, hoping to deal with the complex image noise in real task. Specifically, different from the conventional i.i.d. noise hypothesis on the whole image, we assume that different small patches within the image are with different noise distributions, which largely increases the capacity of the noise model. What’s more, equipped with powerful image prior and elaborately designed inference algorithm, it is able to achieve better performance with not only a slighter CNN-based super-resolved model but also faster speed.

In summary, this paper mainly makes following distributions:

- An unsupervised and blind SISR method is constructed under the probabilistic framework as shown in Fig. 1, which individually seeks an optimized CNN super-resolver for the specific LR image, thus being able to handle the unknown degradation in real scenarios.

- A patch-based non-i.i.d. Gaussian distribution, being with larger capacity than conventional, is proposed to fit the complex real noise. What’s more, the noise variance parameters are automatically updated during inference, leading an adaptively re-weighted loss in each iteration.
- To sufficiently model the image manifold, a deep CNN generator is employed to generate the expected HR image from a latent variable. Besides, the traditional hyper-Laplacian prior is also embedded into such generator as a gradient sparsity prior to constrain the generator parameters. With the elaborately designed Monte Carlo EM algorithm, the image generator can be updated both w.r.t. the latent variable and network parameters in a sound framework as shown in Fig. 1.
- Extensive experiments demonstrate the superiorities of the proposed method on the synthetic and real data sets. It is noteworthy that even with a much slighter CNN generator (0.34M vs. 2.40M) comparing with current SotA method, our method is still able to achieve evident performance gain (about 1dB PSNR) with faster speed.

2 Related Work

In this section, we mainly review and discuss the relevant unsupervised SISR methods to this work. For the purpose of comprehensiveness, we also briefly recap the supervised SISR methods.

Unsupervised methods: The unsupervised methods can be roughly divided into two categories, i.e., interpolation-based and model-based methods. The interpolation-based methods were earliest explored to solve the SISR problem, e.g., spline interpolation [5], bicubic interpolation [24] and other variants [7, 6]. Different from such intuitive interpolated manner, model-based methods represent another research trend. The main idea is to regard the SISR task as an optimization problem under the MAP framework, which contains a data fidelity term and an image prior term. Most of these methods concentrate on exploiting better image prior to alleviate the ill-posedness. Typical traditional image prior includes gradient profile [10], hyper-Laplacian [25, 26], sparsity [12, 11], patch recurrence across scales [27, 28], etc.

With the prevalence of deep learning, DNN is also employed to develop more powerful image prior recently, such as DIP [18], SinGAN [29], DGP [19, 30] and so on. ZSSR [1] proposed a zero-shot SISR method by further exploiting the patch recurrence across scales within a single image using CNN. Also based on such recurrence prior, KernelGAN [17] proposed a blur kernel estimation method for SISR task. On the basis of DIP, DoubleDIP [20, 21] introduced another MLP to generate the blur kernel, and thus made it be able to deal with the blind SISR task. Most notably, DIPFKP [4] constructed an invertible mapping between the anisotropic Gaussian kernel and a tractable latent distribution using normalizing flow [22, 23], and inserted it into the DIP framework as a kernel prior.

Supervised methods: The supervised methods, mainly indicating the learning-based methods in the SISR task, aim to learn a super-resolver through end-to-end training from large amount of pre-simulated LR/HR image pairs. Dong *et al.* [16] firstly proposed to learn an end-to-end CNN mapping from LR to HR images to solve the SISR problem. Later, plenty of CNN architectures elaborately designed for SISR task are proposed, e.g., [31–40]. Besides, different degradation models [41–43] are also widely studied due to their importance in simulating training data, which directly affects its generalization capability in real scenarios. Recently, some unpaired SISR methods [44–46] under pseudo supervision are paid more attentions, mainly because of the fact that real LR images rarely come with the corresponding HR ones in practice.

3 The Proposed Method

3.1 Degradation Model

As is well known, degradation model plays a core role in the SISR problem, which directly determines how to construct the corresponding SISR model. Various degradation models have been proposed in previous research, most of them can be written as a downsampling combined with a subsequent noise contamination process, i.e.,

$$\mathbf{y} = D(\mathbf{x}; \mathbf{k}, \downarrow_s) + \mathbf{n}, \quad (1)$$

where \mathbf{y} and \mathbf{x} denote the LR and HR image, respectively, $D(\mathbf{x}; \mathbf{k}, \downarrow_s)$ represents the downsampling process with blur kernel \mathbf{k} and s -fold downsampler \downarrow_s , and \mathbf{n} is the noise. It should be noted that the real LR image may be also obtained by firstly adding noise and then downsampling the HR

image [43], which makes the noise in LR image more complicated. However, such degradation process can be also equivalently reformulated into the same format with Eq. (1), i.e.,

$$\mathbf{y} = D(\mathbf{x} + \mathbf{n}; \mathbf{k}, \downarrow_s) = D(\mathbf{x}; \mathbf{k}, \downarrow_s) + \hat{\mathbf{n}}, \quad (2)$$

where $\hat{\mathbf{n}} = D(\mathbf{n}; \mathbf{k}, \downarrow_s)$. Thus, we only need to consider the degraded sequence defined in Eq. (1). Furthermore, considering different settings of the kernel \mathbf{k} (e.g, isotropic/anisotropic Gaussian [2, 41]), the downsampler \downarrow_s (e.g., bicubic [31], direct¹ [3]) and their imposed order (i.e., $(\mathbf{x} * \mathbf{k}) \downarrow_s$ [3], $(\mathbf{x} \downarrow_s) * \mathbf{k}$ [42]), where $*$ is the convolution operator, we can obtain multiple different degradation assumptions on the basis of Eq. (1).

Actually, our proposed SISR method presented in the following part is a general image restoration framework and does not depend on any specific degradation model. Therefore, we adopt the most widely used degradation model to construct our SISR method for easy presentation, i.e.,

$$\mathbf{y} = (\mathbf{x} * \mathbf{k}) \downarrow_s^d + \mathbf{n}, \quad (3)$$

where \downarrow_s^d denotes the direct downsampler with scale factor s .

3.2 Probabilistic SISR Model

In this part, based on the degradation assumption defined in Eq. (3), we will build our unsupervised SISR model under the probabilistic framework.

Non-i.i.d. Noise Modeling: Different from the traditional i.i.d. Gaussian noise assumption on the whole image, a novel patch-based non-i.i.d. noise modeling manner is proposed in this work. Specifically, given any observed LR image $\mathbf{y} \in \mathbb{R}^{h \times w}$, where h and w denotes the image height and width, we regard \mathbf{y} as N ($N = hw$) highly overlapped small patches with size $p \times p$. Intuitively, different patches should be with different noise distributions. However, for the i -th image patch centered at y_i , the conventional i.i.d. Gaussian noise hypothesis is sufficient enough for it. Therefore, we have the following formulation for y_i , i.e.,

$$y_i \sim \mathcal{N}(y_i | [(\mathbf{x} * \mathbf{k}) \downarrow_s^d]_i, \lambda_i), \quad i = 1, 2, \dots, N, \quad (4)$$

where λ_i is the noise variance for the i -th image patch. Under such noise assumption, each pixel has its own variance parameter, which largely increases the capacity of the noise distribution when handling complex noise. Note that it naturally degenerates into the i.i.d. Gaussian noise modeling manner by regarding the whole image as a special image patch.

Image Prior Modeling: For the HR image, we employ a deep generator G that parameterized as a CNN to generate it from the latent space, i.e.,

$$\mathbf{x} = G(\mathbf{z}; \boldsymbol{\alpha}), \quad (\boldsymbol{\alpha}, \mathbf{z}) \sim p(\boldsymbol{\alpha}|\mathbf{z})p(\mathbf{z}), \quad (5)$$

where \mathbf{z} and $\boldsymbol{\alpha}$ denote the latent variable and network parameters, $p(\mathbf{z}) = \mathcal{N}(\mathbf{z}|0, \mathbf{I})$ is the probabilistic distribution for latent variable \mathbf{z} . However, as demonstrated in [18], it is very easy for G to overfit onto the image noise due to its very powerful nonlinear fitting capability. Therefore, we introduce the conventional hyper-Laplacian prior to constrain the statistical regularity of the generated HR image by elaborately designing the following conditional distribution:

$$p(\boldsymbol{\alpha}|\mathbf{z}) \propto \exp \left(-\rho \sum_{k=1}^2 |f_k * G(\mathbf{z}; \boldsymbol{\alpha})|^\gamma \right), \quad (6)$$

where $\{f_k\}_{k=1}^2$ are the gradient filters along the horizontal and vertical directions, ρ is a hyper-paramter that controls the relative importance of such prior.

As for the generator G , we follow the ‘‘hourglass’’ architecture in DIP [18] but use a very tiny version that contains much fewer parameters, which largely accelerates its implemented speed. Nevertheless, our method still achieves evidently better performance than current SotA method as shown in Sec. 5.1. And the detailed network architecture can be seen in the supplemental material.

¹Direct downsampler with scale factor s means keeping the upper-left pixel for each distinct $s \times s$ patch and discarding the others.

Kernel Prior Modeling: To construct a complete blind SISR model, it is necessary to introduce some rational kernel priors to guide the kernel estimation. In this work, we assume the kernel to be anisotropic Gaussian kernel, which is sufficient enough in the SISR task as pointed out in [2, 3].

Based on the normalizing flow [22, 23], a data-driven kernel prior, namely FKP (flow-based kernel prior) [4], is proposed recently. The main idea of it is to build a bijection $F(\cdot; \theta)$ with parameter θ between the anisotropic kernel space \mathcal{K} and the pre-assumed latent space \mathcal{Z} , i.e.,

$$\mathbf{k} = F(\xi; \theta), \quad \xi = F^{-1}(\mathbf{k}; \theta), \quad (7)$$

where $\mathbf{k} \sim \mathcal{K}$ is the kernel variable, $\xi \sim \mathcal{Z}$ is the latent variable usually sampled from Gaussian distribution. With large amount of pre-simulated data pairs $\{\xi^j, \mathbf{k}^j\}$, the parameter θ can be optimized by minimizing the negative log-likelihood through end-to-end training.

Let's denote the well-trained bijection as $F(\xi; \theta^0)$, where θ^0 is the network parameter after optimization. Naturally, by fixing θ^0 , such bijection can be directly used as a kernel prior in our model:

$$\mathbf{k} = F(\xi; \theta^0), \quad \xi \sim \mathcal{N}(\xi|0, \mathbf{I}). \quad (8)$$

For notation convenience, we briefly denote $F(\xi; \theta^0)$ as $F(\xi)$ in the following presentation.

3.3 MAP Estimation

According to Eqs. (4)-(8), a full probabilistic model is constructed. Under the MAP framework, our goal turns to maximize the following posterior, i.e.,

$$p(\alpha, \xi, \lambda | \mathbf{y}) \propto \int p(\mathbf{y} | \alpha, \xi, \lambda, \mathbf{z}) p(\alpha | \mathbf{z}) p(\mathbf{z}) d\mathbf{z} p(\xi). \quad (9)$$

Taking the logarithm of both sides of Eq. (9), we have the following maximization problem:

$$\begin{aligned} \max_{\alpha, \xi, \lambda} \log p(\alpha, \xi, \lambda | \mathbf{y}) &= \log \int p(\mathbf{y} | \alpha, \xi, \lambda, \mathbf{z}) p(\alpha | \mathbf{z}) p(\mathbf{z}) d\mathbf{z} + \log p(\xi) + \text{const} \\ &\triangleq \mathcal{L}(\mathbf{y}; \alpha, \xi, \lambda). \end{aligned} \quad (10)$$

4 Inference Algorithm

Inspired by the alternative back-propagation [47, 48], we design a Monte Carlo expectation-maximization (EM) algorithm [49] to solve the problem of Eq. (10), which alternately samples the latent variable \mathbf{z} from its posterior $p(\mathbf{z} | \mathbf{y})$ in E-Step and updates the model parameters $\{\alpha, \xi, \lambda\}$ in M-Step. And the whole inference framework is illustrated in Fig. 1.

E-Step: Let $\{\alpha_{\text{old}}, \xi_{\text{old}}, \lambda_{\text{old}}\}$ and $p_{\text{old}}(\mathbf{z} | \mathbf{y})$ denote current model parameters and the posterior under them, we can sample \mathbf{z} from $p_{\text{old}}(\mathbf{z} | \mathbf{y})$ using Langevin dynamics [50]:

$$\begin{aligned} \mathbf{z}^{(\tau+1)} &= \mathbf{z}^{(\tau)} + \frac{\delta^2}{2} \left[\frac{\partial}{\partial \mathbf{z}} \log p_{\text{old}}(\mathbf{z} | \mathbf{y}) \right] \Big|_{\mathbf{z}=\mathbf{z}^{(\tau)}} + \delta \zeta^{(\tau)} \\ &= \mathbf{z}^{(\tau)} - \frac{\delta^2}{2} \left[\frac{\partial}{\partial \mathbf{z}} g(\mathbf{z}) \right] \Big|_{\mathbf{z}=\mathbf{z}^{(\tau)}} + \delta \zeta^{(\tau)}, \end{aligned} \quad (11)$$

where

$$g(\mathbf{z}) = \frac{1}{2} \left\| \frac{1}{\lambda_{\text{old}}} \odot \left\{ [\mathbf{y} - G(\mathbf{z}; \alpha_{\text{old}}) * F(\xi_{\text{old}})] \downarrow_s^d \right\} \right\|_2^2 + \rho \sum_{k=1}^2 |f_k * G(\mathbf{z}; \alpha_{\text{old}})|^\gamma + \frac{1}{2} \|\mathbf{z}\|_2^2, \quad (12)$$

τ indexes the time step for Langevin dynamics, δ denotes the step size, ζ is the Gaussian white noise used to prevent trapping into local modes. And \odot represents the Hadamard product. Note that $g(\mathbf{z})$ is calculated based on the fact that $\frac{\partial}{\partial \mathbf{z}} \log p_{\text{old}}(\mathbf{z} | \mathbf{y}) = \frac{\partial}{\partial \mathbf{z}} \log p_{\text{old}}(\mathbf{z}, \mathbf{y})$.

In practice, a small trick to accelerate the convergence speed of Monte Carlo sampling in Eq. (11) is to start from the previous updated \mathbf{z} in each learning iteration. And we empirically found that it performs very stably and well by simply sampling 5 times according to Eq. (11).

Algorithm 1 Inference procedure for our proposed SISR method

Input: observed LR image, hyper-parameters: $\gamma = 2/3$, $\rho = 0.25$, $\delta = 0.05$, $p = 11$.

Output: the super-resolved HR image I^{HR} .

- 1: Initialize the model parameters $\{\alpha, \xi, \lambda\}$ and the latent variable z .
 - 2: **while** not converged **do**
 - 3: **E-Step:** Sample the latent variable z from $p_{\text{old}}(z|\mathbf{y})$ following Eq. (11).
 - 4: **M-Step:** (a) Update kernel parameter ξ with fixed α and λ according to Eq. (15).
 - 5: (b) Update generator α with fixed ξ and λ according to Eq. (15).
 - 6: (c) Update noise variance parameter λ with fixed α and ξ according to Eq. (16).
 - 7: **end while**
 - 8: $I^{\text{HR}} = G(z; \alpha)$.
-

M-Step: Denote the sampled latent variable in E-step as \tilde{z} , M-Step aims to maximize the approximate lower bound of $\mathcal{L}(\mathbf{y}; \alpha, \xi, \lambda)$ w.r.t. the model parameters $\{\alpha, \xi, \lambda\}$, i.e.,

$$\begin{aligned} \max_{\alpha, \xi, \lambda} Q(\alpha, \xi, \lambda) &= \int p_{\text{old}}(z|\mathbf{y}) \log p(\mathbf{y}|\alpha, \xi, \lambda, z) p(\alpha|z) p(z) dz + \log p(\xi) \\ &\approx \log p(\mathbf{y}|\alpha, \xi, \lambda, \tilde{z}) p(\alpha|\tilde{z}) p(\tilde{z}) + \log p(\xi). \end{aligned} \quad (13)$$

Equivalently, Eq. (13) can be further reformulated into a minimization problem as follows:

$$\min_{\alpha, \xi, \lambda} E(\alpha, \xi, \lambda) = \frac{1}{2} \left\| \frac{1}{\lambda} \odot \left\{ [\mathbf{y} - G(\tilde{z}; \alpha) * F(\xi)] \downarrow_s^d \right\} \right\|_2^2 + \rho \sum_{k=1}^2 |f_k * G(\tilde{z}; \alpha)|^\gamma + \frac{1}{2} \|\xi\|_2^2. \quad (14)$$

To solve Eq. (14), we alternately update the model parameters α , ξ and λ . Specifically, for α or ξ , they can be directly optimized by gradient descent based on the back-propagation (BP) algorithm [51]:

$$\mathbf{W}_{\text{new}} = \mathbf{W}_{\text{old}} - \eta \frac{\partial}{\partial \mathbf{W}} E(\alpha, \xi, \lambda), \quad \mathbf{W} \in \{\alpha, \xi\}, \quad (15)$$

where η is the learning rate. Note that the first term of (14) can be regarded as re-weighted L_2 loss with weight $\frac{1}{\lambda}$, which is automatically updated in each iteration.

For the noise variance map λ , we consider λ_i in the $p \times p$ patch centered at the i -th pixel. Fortunately, based on the i.i.d. Gaussian noise assumption within this image patch, we can obtain the following closed-form solution for λ_i by simply setting its derivative to zero, i.e.,

$$\lambda_i = \frac{1}{p^2} \sum_{j \in N(i)} \left\{ y_j - \left[(G(\tilde{z}; \alpha_{\text{old}}) * F(\xi_{\text{old}})) \downarrow_s^d \right]_j \right\}^2, \quad (16)$$

where $N(i)$ is the index set of the pixels in the $p \times p$ patch centered at i . Note that Eq. (16) can be fastly implemented through average filtering on the square of the residual term. And the detailed description of the proposed EM algorithm is presented in Algorithm 1.

Remark: In our model, we also employed a DNN (i.e., the generator G in Eq. (5)) to generate the HR image from latent space like current DIP-based methods (e.g., DIP [18], DoubleDIP [20, 21] and DIPFKP [4]). Nevertheless, this work is initially inspired by different motivations with them. Firstly, this paper mainly aims to provide a general modeling and inference framework focusing on how to embed DNNs into conventional probabilistic modeling methods, so as to largely extend such methods with the aid of the powerful nonlinear fitting capabilities of DNNs. Even though we only consider the SISR task in this work, the proposed method can be naturally extended to deal with general low-level vision tasks. What's more, it is also possible to use better image prior or kernel prior instead of the hyper-Laplacian or FKP [4] in our framework. Secondly, the employment of DNN in our model is mainly motivated by one widely used hypothesis in Bayesian modeling, i.e., the observed data can be generated from a latent variable. During inference, the network parameters of the generator G and the latent variable z are alternately updated using the designed EM algorithm. However, to the best of our knowledge, DIP-based methods expect to exploit whether is the handcrafted structure of CNN able to capture the image statistics with *fixed* latent noise z . Thirdly, our model employs a more rational non-i.i.d. noise modeling manner, and demonstrates obvious superiorities when encountering more complex noise, e.g., the spatially variant noise or the camera sensor noise as shown in Sec. 5.

Table 1: Comparision results of different methods on the model size (K) and the running time (s).

Methods	ZSSR [1]			DIPFKP [4]			USRCN (ours)		
Scale	$\times 2$	$\times 3$	$\times 4$	$\times 2$	$\times 3$	$\times 4$	$\times 2$	$\times 3$	$\times 4$
Time (s)	128	120	117	78	152	261	23	43	72
# parameters (K)	225			2396			335		



Figure 2: From left to right: (a) variance map M for noise Case 2; (b) clean image; (c) noisy image obtained by adding the camera sensor noise of Case 3 on (b); (d) the absolute residual (or noise) between (b) and (c).

5 Experimental results

We conduct some experiments to verify the effectiveness of the proposed method on the synthetic and real data sets. For easy presentation, we briefly denote our Unsupervised image Super-Resolution method under Complex Noise as USRCN in the following parts. Note that more visual comparisons and the analyses of the hyper-paramters are put into the supplemental material due to page limitation.

Training settings: Throughout the whole experiments, we empirically set the hyper-paramters ρ and γ as 0.20 and $2/3$, respectively. In the M-Step during inference, the Adam [52] algorithm with default settings is used to update the model parameters α and ξ instead of the original gradient descent strategy in Eq. (15). The learning rates for α and ξ are set as $2e-3$ and $5e-1$ in the whole algorithm, respectively. As for the patch size p in the noise modeling, we set it as 11. For fair comparison, all the quantitative results are averaged by running the algorithm 5 times with different random seeds.

Compared methods: To better evaluate USRCN, we consider five compared methods, including one supervised deep learning (DL)-based method RCAN [34] and four model-based methods, i.e., SelfExSR [53], ZSSR [1], DoubleDIP [21] and DIPFKP [4]. Specifically, RCAN is the current SotA method under PSNR metric for bicubic degradation; SelfExSR is a traditional self-similarity oriented method with geometric variation for the internal patches; ZSSR is a non-blind zero-shot method by exploiting the patch recurrence across scales in a single image; DoubleDIP and DIPFKP are both blind SISR methods but with different kernel priors. It is worth noting that ZSSR, DoubleDIP and DIPFKP are also DL-based, because they all employ the deep CNN to model the image prior.


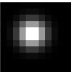

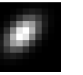
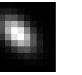
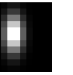
5.1 Comparisons on model size and running time

For the model-based unsupervised SISR methods, one of the main limitations for them to be deployed on real hardwares are the large model size, which also leads to slow implemented speed. In the proposed USRCN, we empirically find that a very tiny CNN is powerful enough to handle the SISR task in our framework. Table 1 lists the comparison results on model size (number of parameters) and running time with two current DL-based methods, i.e., ZSSR and DIPFKP. Since DoubleDIP and DIPFKP have very similar model size and implemented speed, we do not compare with it. For the running time, we fixed the LR image size as 256×256 and counted the elapsed time of super-resolving it to the size of 512×512 , 768×768 and 1024×1024 with scale factor 2, 3 and 4, respectively. And all the results in Table 1 were tested on a Tesla V100 GPU. From Table 1, it can be easily observed that USRCN is with obvious superiorities than the SotA method DIPFKP both on the model size (about 7 times smaller) and the implemented speed (about 4 times faster), which substantiates its high practical value in real applications.

5.2 Evaluation on Synthetic Data

In this part, we quantitatively evaluate different methods on two commonly-used data sets, i.e., Set14 [54] and CBSD68 [55], which contains abundant structures and textures. The LR images are synthesized via Eq. (3). For the purpose of conducting a thorough comparison, we consider diverse degradations combined with different blur kernels and noise types. As for the blur kernels, 2 isotropic

Table 2: PSNR/SSIM results of the compared methods under different degraded combinations on Set14. The best results are highlighted in **bold**. The **gray** results indicate unfair comparison due to mismatched degradations.

Noise types	Methods	Scale factors	Blur Kernels					
								
Case 1	RCAN [34]	$\times 2$	25.05 / 0.698	25.01 / 0.690	24.79 / 0.679	24.61 / 0.661	25.07 / 0.690	24.81 / 0.676
	SelfExSR [53]	$\times 2$	24.90 / 0.699	24.86 / 0.691	24.65 / 0.680	24.47 / 0.662	24.91 / 0.690	24.67 / 0.677
	ZSSR [1]	$\times 2$	24.73 / 0.715	24.81 / 0.713	24.79 / 0.706	24.58 / 0.691	25.17 / 0.721	24.85 / 0.706
	DoubleDIP [21]	$\times 2$	24.50 / 0.674	24.87 / 0.686	24.88 / 0.665	25.27 / 0.693	24.96 / 0.687	24.69 / 0.680
	DIPFKP [4]	$\times 2$	27.67 / 0.764	27.39 / 0.752	26.95 / 0.743	26.77 / 0.731	26.80 / 0.728	26.84 / 0.737
	USRCN	$\times 2$	29.36 / 0.825	28.83 / 0.807	28.34 / 0.802	27.93 / 0.780	28.02 / 0.778	28.24 / 0.785
	RCAN [34]	$\times 3$	21.54 / 0.535	21.83 / 0.547	22.06 / 0.549	22.05 / 0.540	22.64 / 0.588	22.15 / 0.556
	SelfExSR [53]	$\times 3$	21.55 / 0.545	21.75 / 0.553	22.01 / 0.557	21.93 / 0.543	22.46 / 0.588	22.02 / 0.560
	ZSSR [1]	$\times 3$	21.42 / 0.549	21.46 / 0.550	21.67 / 0.554	21.41 / 0.535	21.96 / 0.579	21.69 / 0.559
	DoubleDIP [21]	$\times 3$	21.22 / 0.523	22.21 / 0.566	21.75 / 0.549	22.31 / 0.566	21.55 / 0.546	21.94 / 0.551
	DIPFKP [4]	$\times 3$	27.06 / 0.735	26.89 / 0.728	26.12 / 0.698	25.77 / 0.684	26.00 / 0.688	26.15 / 0.690
	USRCN	$\times 3$	27.87 / 0.774	28.02 / 0.771	26.83 / 0.736	26.69 / 0.726	26.81 / 0.729	26.76 / 0.729
	RCAN [34]	$\times 4$	19.20 / 0.443	19.53 / 0.454	20.44 / 0.484	20.42 / 0.473	20.97 / 0.520	20.46 / 0.488
	SelfExSR [53]	$\times 4$	19.65 / 0.461	19.84 / 0.470	20.49 / 0.494	20.42 / 0.482	20.91 / 0.524	20.48 / 0.497
	ZSSR [1]	$\times 4$	19.74 / 0.471	19.75 / 0.473	19.93 / 0.476	19.71 / 0.463	20.11 / 0.500	19.94 / 0.482
	DoubleDIP [21]	$\times 4$	19.31 / 0.440	19.57 / 0.439	19.63 / 0.441	20.51 / 0.481	20.06 / 0.468	20.11 / 0.462
	DIPFKP [4]	$\times 4$	25.91 / 0.697	25.97 / 0.694	24.87 / 0.658	24.95 / 0.654	25.10 / 0.645	25.14 / 0.660
	USRCN	$\times 4$	26.34 / 0.709	26.37 / 0.715	26.12 / 0.697	26.13 / 0.693	26.22 / 0.695	26.08 / 0.694
Case 2	RCAN [34]	$\times 2$	24.81 / 0.661	24.77 / 0.654	24.53 / 0.639	24.38 / 0.625	24.83 / 0.653	24.56 / 0.638
	SelfExSR [53]	$\times 2$	24.98 / 0.716	24.94 / 0.708	24.73 / 0.697	24.55 / 0.679	24.99 / 0.708	24.76 / 0.694
	ZSSR [1]	$\times 2$	24.75 / 0.704	24.81 / 0.702	24.77 / 0.696	24.60 / 0.683	25.08 / 0.706	24.81 / 0.694
	DoubleDIP [21]	$\times 2$	24.72 / 0.677	25.14 / 0.690	24.38 / 0.651	25.07 / 0.681	25.34 / 0.694	24.74 / 0.673
	DIPFKP [4]	$\times 2$	27.62 / 0.758	27.31 / 0.745	26.77 / 0.738	26.46 / 0.647	26.76 / 0.725	26.77 / 0.731
	USRCN	$\times 2$	28.55 / 0.800	28.19 / 0.786	27.91 / 0.780	27.54 / 0.761	27.53 / 0.760	27.61 / 0.765
	RCAN [34]	$\times 3$	21.46 / 0.514	21.74 / 0.525	21.97 / 0.527	21.96 / 0.617	22.53 / 0.563	22.04 / 0.532
	SelfExSR [53]	$\times 3$	21.58 / 0.557	21.79 / 0.566	22.05 / 0.570	21.97 / 0.556	22.51 / 0.603	22.07 / 0.573
	ZSSR [1]	$\times 3$	21.44 / 0.545	21.48 / 0.545	21.70 / 0.550	21.47 / 0.533	21.93 / 0.570	21.69 / 0.554
	DoubleDIP [21]	$\times 3$	21.81 / 0.532	21.81 / 0.523	21.75 / 0.526	22.27 / 0.546	21.40 / 0.521	22.32 / 0.544
	DIPFKP [4]	$\times 3$	26.93 / 0.726	26.74 / 0.720	25.95 / 0.686	25.73 / 0.674	25.90 / 0.678	25.85 / 0.678
	USRCN	$\times 3$	27.32 / 0.749	27.46 / 0.747	26.49 / 0.717	26.35 / 0.707	26.51 / 0.710	26.51 / 0.713
	RCAN [34]	$\times 4$	19.16 / 0.425	19.48 / 0.436	20.34 / 0.464	20.34 / 0.454	20.87 / 0.499	20.37 / 0.468
	SelfExSR [53]	$\times 4$	19.67 / 0.470	19.87 / 0.479	20.52 / 0.503	20.45 / 0.492	20.94 / 0.534	20.51 / 0.506
	ZSSR [1]	$\times 4$	19.76 / 0.468	19.77 / 0.470	19.95 / 0.473	19.76 / 0.459	20.14 / 0.492	19.99 / 0.476
	DoubleDIP [21]	$\times 4$	18.49 / 0.378	18.67 / 0.386	19.91 / 0.435	20.25 / 0.454	20.19 / 0.457	20.01 / 0.443
	DIPFKP [4]	$\times 4$	25.48 / 0.681	25.82 / 0.681	24.74 / 0.648	24.66 / 0.640	24.92 / 0.648	25.01 / 0.645
	USRCN	$\times 4$	26.39 / 0.711	26.43 / 0.720	25.63 / 0.675	25.58 / 0.671	25.66 / 0.673	25.50 / 0.672
Case 3	RCAN [34]	$\times 2$	24.51 / 0.657	24.54 / 0.652	24.41 / 0.645	24.27 / 0.630	24.64 / 0.652	24.41 / 0.641
	SelfExSR [53]	$\times 2$	24.35 / 0.657	24.37 / 0.652	24.24 / 0.644	24.10 / 0.629	24.47 / 0.651	24.24 / 0.641
	ZSSR [1]	$\times 2$	24.69 / 0.698	24.73 / 0.695	24.70 / 0.690	24.53 / 0.678	24.94 / 0.696	24.69 / 0.688
	DoubleDIP [21]	$\times 2$	24.82 / 0.659	25.26 / 0.678	24.60 / 0.636	25.02 / 0.665	25.11 / 0.675	24.76 / 0.664
	DIPFKP [4]	$\times 2$	27.06 / 0.743	26.97 / 0.733	26.49 / 0.729	26.49 / 0.719	26.56 / 0.718	26.58 / 0.720
	USRCN	$\times 2$	27.86 / 0.781	27.74 / 0.770	27.47 / 0.766	27.24 / 0.752	27.34 / 0.751	27.23 / 0.742
	RCAN [34]	$\times 3$	21.37 / 0.516	21.55 / 0.522	21.85 / 0.527	21.79 / 0.518	22.23 / 0.548	21.86 / 0.528
	SelfExSR [53]	$\times 3$	21.28 / 0.518	21.44 / 0.523	21.71 / 0.528	21.65 / 0.518	22.05 / 0.548	21.71 / 0.529
	ZSSR [1]	$\times 3$	21.59 / 0.552	21.61 / 0.553	21.76 / 0.554	21.61 / 0.545	21.94 / 0.567	21.78 / 0.556
	DoubleDIP [21]	$\times 3$	21.02 / 0.500	21.68 / 0.529	21.28 / 0.502	21.91 / 0.520	21.78 / 0.529	21.68 / 0.513
	DIPFKP [4]	$\times 3$	25.40 / 0.677	25.45 / 0.673	25.10 / 0.653	25.00 / 0.644	24.94 / 0.643	25.08 / 0.649
	USRCN	$\times 3$	26.18 / 0.721	26.24 / 0.719	25.92 / 0.697	25.84 / 0.690	25.92 / 0.691	25.94 / 0.694
	RCAN [34]	$\times 4$	19.48 / 0.436	19.63 / 0.442	20.22 / 0.461	20.22 / 0.456	20.59 / 0.482	20.24 / 0.463
	SelfExSR [53]	$\times 4$	19.59 / 0.444	19.72 / 0.450	20.24 / 0.467	20.20 / 0.461	20.55 / 0.487	20.23 / 0.469
	ZSSR [1]	$\times 4$	19.80 / 0.475	19.82 / 0.476	19.94 / 0.478	19.69 / 0.469	19.98 / 0.488	19.94 / 0.480
	DoubleDIP [21]	$\times 4$	19.15 / 0.418	19.81 / 0.446	18.72 / 0.381	19.72 / 0.427	19.93 / 0.441	19.74 / 0.429
	DIPFKP [4]	$\times 4$	24.13 / 0.623	24.18 / 0.622	23.92 / 0.597	23.91 / 0.594	23.88 / 0.592	23.88 / 0.597
	USRCN	$\times 4$	24.59 / 0.661	24.72 / 0.663	24.81 / 0.649	24.86 / 0.646	24.90 / 0.647	24.77 / 0.648

Gaussian kernels with different widths (i.e., 1.2 and 2.0) and 4 anisotropic Gaussian kernels are chosen. Furthermore, we consider three noise types based on such 6 kernels as follows:

- Case 1: Gaussian noise with noise level 2.55, which is widely used in current SISR literatures.
- Case 2: Spatially variant noise generated through $n = \hat{n} \odot M$, where $\hat{n} \sim \mathcal{N}(\hat{n}|0, I)$, M is a variance map (see Fig. 2 (a)), and \odot is the Hadamard product.
- Case 3: Camera sensor noise simulated by [56], one typical example is shown in Fig. 2 (b)-(d).

Especially, the noise in Case 3 is very close to the real camera noise, and thus suitable to be used to evaluate different methods for the degradations with complex real noise. The PSNR and SSIM [57] averaged on the whole data set are used as quantitative metrics. Note that these two metrics are both evaluated in the luminance channel due to our sensitivity to this channel.

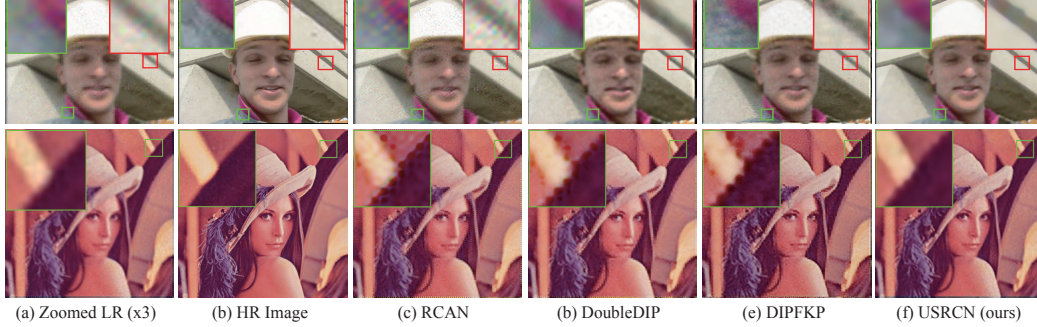


Figure 3: Visual super-resolved results of different methods for the degradations under the spatially variant noise of Case 2 (top row) and the camera sensor noise of Case 3 (bottom row) with scale factor 3 on Set 14.

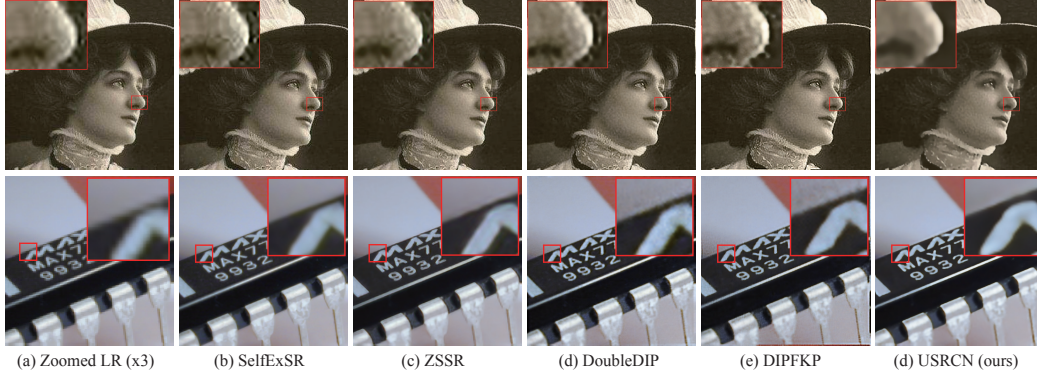


Figure 4: Two typical visual results of different methods on the real LR images with scale factor 3.

Table 2 lists the PSNR/SSIM results of different methods for diverse degradations on Set14. The performance comparisons on CBSD68 can be seen in the supplemental material. From Table 2, we can see that the proposed USRCN achieves better performance than the other methods for all the degradations. The PSNR gain on current SotA method DIPFKP is about 1dB in most cases, which is a relatively large improvement in SISR task. Specifically, for the blur kernels, the superiorities are more obvious in the more challenged anisotropic Gaussian kernel cases. As for the noise, USRCN demonstrates evident advantages in all the three noise types. Therefore, it is rational to believe that the proposed USRCN is capable of dealing with more complex degradations.

Two typical visual results on the noise Case 2 and noise Case 3 are shown in Fig. 3. Note that we only display the four best methods due to page limitation. In the noise Case 2, the recovered results of RCAN and DIPFKP both contain some obvious noises, while DoubleDIP obtains over-smoothed image. In the noise Case 3, all the three compared methods all lead to some artifacts, possibly because their i.i.d. Gaussian noise assumption largely deviates from the true noise distribution. However, our USRCN is able to remove most of the noises and preserve sharper edges in both of such spatially variant or camera sensor noise cases, mainly due to its proper non-i.i.d. noise modeling manner.

5.3 Evaluation on Real Data

To further justify the effectiveness of USRCN in real SISR task, we evaluate it on the RealSRSet [43], which contains 20 real images from internet or existing testing data sets [58–61]. Fig. 4 shows two visual examples, and more results can be seen in the supplemental material. It can be easily seen that the proposed USRCN achieves obviously better qualitative results. Specifically, for the old photo that contains heavy noise (top row of Fig. 4), the other compared methods all fail to remove the noise. For the commonly-used “chip” example (bottom row of Fig. 4) in the real SISR task, USRCN evidently achieve much sharper and cleaner result. In summary, taking all the model size, implemented speed (see Sec. 5.1) and such visual results into consideration, it should be rational to say the proposed method takes the SISR research closer toward the real-world industrial applications.

6 Conclusions

In this paper, we have designed a new unsupervised SISR method. To better encode the complex real noise, a full probabilistic SISR model is constructed under a novel patch-based non-i.i.d. noise

assumption. Besides, a deep CNN generator embedded with the conventional hyper-Laplacian prior on image gradients is also employed to recover the HR image. With the elaborately designed Monte Carlo EM algorithm, our method is able to achieve promising performance on synthetic and real data sets even only with a very tiny CNN model. Therefore, we believe that this work paves the way toward the real SISR problem with complex degradations. However, due to huge computational burden led by the optimization-based learning paradigm, it is very hard to meet the online processing requirements in some real applications. We will focus on such limitation in the future work.

By the way, as a traditional task in computer vision, SISR has largely improved our life in various areas, such as video enhancement, medical imaging, surveillance imaging and so on. This work manages to propose a more robust SISR method toward the unknown and complex degradations, and will further facilitate the applications of SISR in our life. As for the negative impacts, this work does not present any foreseeable negative societal influences.

References

- [1] Assaf Shocher, Nadav Cohen, and Michal Irani. “zero-shot” super-resolution using deep internal learning. In *Proceedings of the IEEE/CVF Conference on Computer Vision and Pattern Recognition (CVPR)*, pages 3118–3126, 2018.
- [2] Gernot Riegler, Samuel Schuler, Matthias Ruther, and Horst Bischof. Conditioned regression models for non-blind single image super-resolution. In *Proceedings of the IEEE/CVF International Conference on Computer Vision (ICCV)*, pages 522–530, 2015.
- [3] Kai Zhang, Luc Van Gool, and Radu Timofte. Deep unfolding network for image super-resolution. In *Proceedings of the IEEE/CVF Conference on Computer Vision and Pattern Recognition (CVPR)*, pages 3217–3226, 2020.
- [4] Jingyun Liang, Kai Zhang, Shuhang Gu, Luc Van Gool, and Radu Timofte. Flow-based kernel prior with application to blind super-resolution. *arXiv preprint arXiv:2103.15977*, 2021.
- [5] Hsieh Hou and H Andrews. Cubic splines for image interpolation and digital filtering. *IEEE Transactions on Acoustics, Speech, and Signal Processing*, 26(6):508–517, 1978.
- [6] Philippe Thévenaz, Thierry Blu, and Michael Unser. Image interpolation and resampling. *Handbook of Medical Imaging, Processing and Analysis*, 1(1):393–420, 2000.
- [7] Xin Li and Michael T Orchard. New edge-directed interpolation. *IEEE Transactions on Image Processing (TIP)*, 10(10):1521–1527, 2001.
- [8] Radu Timofte, Vincent De Smet, and Luc Van Gool. A+: Adjusted anchored neighborhood regression for fast super-resolution. In *Asian Conference on Computer Vision (ACCV)*, pages 111–126. Springer, 2014.
- [9] Stefan Roth and Michael J Black. Fields of experts: A framework for learning image priors. In *IEEE Conference on Computer Vision and Pattern Recognition (CVPR)*, volume 2, pages 860–867. IEEE, 2005.
- [10] Jian Sun, Zongben Xu, and Heung-Yeung Shum. Image super-resolution using gradient profile prior. In *Proceedings of the IEEE/CVF Conference on Computer Vision and Pattern Recognition (CVPR)*, pages 1–8. IEEE, 2008.
- [11] Weisheng Dong, Lei Zhang, Guangming Shi, and Xin Li. Nonlocally centralized sparse representation for image restoration. *IEEE transactions on Image Processing (TIP)*, 22(4):1620–1630, 2012.
- [12] Kwang In Kim and Younghee Kwon. Single-image super-resolution using sparse regression and natural image prior. *IEEE Transactions on Pattern Analysis and Machine Intelligence (TPAMI)*, 32(6):1127–1133, 2010.
- [13] Yunjin Chen and Thomas Pock. Trainable nonlinear reaction diffusion: A flexible framework for fast and effective image restoration. *IEEE Transactions on Pattern Analysis and Machine Intelligence (TPAMI)*, 39(6):1256–1272, 2016.

- [14] William T Freeman, Egon C Pasztor, and Owen T Carmichael. Learning low-level vision. *International Journal of Computer Vision (IJCV)*, 40(1):25–47, 2000.
- [15] Simon Baker and Takeo Kanade. Limits on super-resolution and how to break them. *IEEE Transactions on Pattern Analysis and Machine Intelligence (TPAMI)*, 24(9):1167–1183, 2002.
- [16] Chao Dong, Chen Change Loy, Kaiming He, and Xiaoou Tang. Learning a deep convolutional network for image super-resolution. In *Proceedings of the European Conference on Computer Vision (ECCV)*, pages 184–199. Springer, 2014.
- [17] Sefi Bell-Kligler, Assaf Shocher, and Michal Irani. Blind super-resolution kernel estimation using an internal-gan. In *Advances in Neural Information Processing Systems (NeurIPS)*, volume 32, pages 284–293, 2019.
- [18] Dmitry Ulyanov, Andrea Vedaldi, and Victor Lempitsky. Deep image prior. In *Proceedings of the IEEE/CVF Conference on Computer Vision and Pattern Recognition (CVPR)*, pages 9446–9454, 2018.
- [19] Xingang Pan, Xiaohang Zhan, Bo Dai, Dahua Lin, Chen Change Loy, and Ping Luo. Exploiting deep generative prior for versatile image restoration and manipulation. In *European Conference on Computer Vision (ECCV)*, pages 262–277. Springer, 2020.
- [20] Yosef Gandelsman, Assaf Shocher, and Michal Irani. "double-dip": Unsupervised image decomposition via coupled deep-image-priors. In *Proceedings of the IEEE/CVF Conference on Computer Vision and Pattern Recognition (CVPR)*, pages 11026–11035, 2019.
- [21] Dongwei Ren, Kai Zhang, Qilong Wang, Qinghua Hu, and Wangmeng Zuo. Neural blind deconvolution using deep priors. In *Proceedings of the IEEE/CVF Conference on Computer Vision and Pattern Recognition (CVPR)*, pages 3341–3350, 2020.
- [22] Laurent Dinh, David Krueger, and Yoshua Bengio. Nice: Non-linear independent components estimation. In *ICLR (Workshop)*, 2014.
- [23] Laurent Dinh, Jascha Sohl-Dickstein, and Samy Bengio. Density estimation using real nvp. In *ICLR*, 2016.
- [24] Robert Keys. Cubic convolution interpolation for digital image processing. *IEEE Transactions on Acoustics, Speech, and Signal Processing*, 29(6):1153–1160, 1981.
- [25] Marshall F Tappen Bryan C Russell and William T Freeman. Exploiting the sparse derivative prior for super-resolution and image demosaicing. In *Proceedings of Third International Workshop Statistical and Computational Theories of Vision (SCTV)*, 2003.
- [26] Dilip Krishnan and Rob Fergus. Fast image deconvolution using hyper-laplacian priors. *Advances in Neural Information Processing Systems*, 22:1033–1041, 2009.
- [27] Daniel Glasner, Shai Bagon, and Michal Irani. Super-resolution from a single image. In *Proceedings of the IEEE/CVF International Conference on Computer Vision (ICCV)*, pages 349–356. IEEE, 2009.
- [28] Tomer Michaeli and Michal Irani. Nonparametric blind super-resolution. In *Proceedings of the IEEE/CVF International Conference on Computer Vision (ICCV)*, pages 945–952, 2013.
- [29] Tamar Rott Shaham, Tali Dekel, and Tomer Michaeli. Singan: Learning a generative model from a single natural image. In *Proceedings of the IEEE/CVF International Conference on Computer Vision (ICCV)*, pages 4570–4580, 2019.
- [30] Jinjin Gu, Yujun Shen, and Bolei Zhou. Image processing using multi-code gan prior. In *Proceedings of the IEEE/CVF Conference on Computer Vision and Pattern Recognition (CVPR)*, pages 3012–3021, 2020.
- [31] Jiwon Kim, Jung Kwon Lee, and Kyoung Mu Lee. Accurate image super-resolution using very deep convolutional networks. In *Proceedings of the IEEE conference on Computer Vision and Pattern Recognition (CVPR)*, pages 1646–1654, 2016.

- [32] Kai Zhang, Wangmeng Zuo, Yunjin Chen, Deyu Meng, and Lei Zhang. Beyond a gaussian denoiser: Residual learning of deep cnn for image denoising. *IEEE Transactions on Image Processing (TIP)*, 26(7):3142–3155, 2017.
- [33] Ying Tai, Jian Yang, Xiaoming Liu, and Chunyan Xu. Memnet: A persistent memory network for image restoration. In *Proceedings of the IEEE/CVF International Conference on Computer Vision (ICCV)*, pages 4539–4547, 2017.
- [34] Yulun Zhang, Kunpeng Li, Kai Li, Lichen Wang, Bineng Zhong, and Yun Fu. Image super-resolution using very deep residual channel attention networks. In *Proceedings of the European conference on computer vision (ECCV)*, pages 286–301, 2018.
- [35] Xintao Wang, Ke Yu, Chao Dong, and Chen Change Loy. Recovering realistic texture in image super-resolution by deep spatial feature transform. In *Proceedings of the IEEE conference on Computer Vision and Pattern Recognition (CVPR)*, pages 606–615, 2018.
- [36] Tao Dai, Jianrui Cai, Yongbing Zhang, Shu-Tao Xia, and Lei Zhang. Second-order attention network for single image super-resolution. In *Proceedings of the IEEE/CVF Conference on Computer Vision and Pattern Recognition (CVPR)*, pages 11065–11074, 2019.
- [37] Xiangyu He, Zitao Mo, Peisong Wang, Yang Liu, Mingyuan Yang, and Jian Cheng. Ode-inspired network design for single image super-resolution. In *Proceedings of the IEEE/CVF Conference on Computer Vision and Pattern Recognition (CVPR)*, pages 1732–1741, 2019.
- [38] Xuecai Hu, Haoyuan Mu, Xiangyu Zhang, Zilei Wang, Tieniu Tan, and Jian Sun. Meta-sr: A magnification-arbitrary network for super-resolution. In *Proceedings of the IEEE/CVF Conference on Computer Vision and Pattern Recognition (CVPR)*, pages 1575–1584, 2019.
- [39] Jie Liu, Wenjie Zhang, Yuting Tang, Jie Tang, and Gangshan Wu. Residual feature aggregation network for image super-resolution. In *Proceedings of the IEEE/CVF Conference on Computer Vision and Pattern Recognition (CVPR)*, pages 2359–2368, 2020.
- [40] Yiqun Mei, Yuchen Fan, Yuqian Zhou, Lichao Huang, Thomas S Huang, and Honghui Shi. Image super-resolution with cross-scale non-local attention and exhaustive self-exemplars mining. In *Proceedings of the IEEE/CVF Conference on Computer Vision and Pattern Recognition (CVPR)*, pages 5690–5699, 2020.
- [41] Kai Zhang, Wangmeng Zuo, and Lei Zhang. Learning a single convolutional super-resolution network for multiple degradations. In *Proceedings of the IEEE Conference on Computer Vision and Pattern Recognition (CVPR)*, pages 3262–3271, 2018.
- [42] Kai Zhang, Wangmeng Zuo, and Lei Zhang. Deep plug-and-play super-resolution for arbitrary blur kernels. In *Proceedings of the IEEE/CVF Conference on Computer Vision and Pattern Recognition (CVPR)*, pages 1671–1681, 2019.
- [43] Kai Zhang, Jingyun Liang, Luc Van Gool, and Radu Timofte. Designing a practical degradation model for deep blind image super-resolution. *arXiv preprint arXiv:2103.14006*, 2021.
- [44] Yuan Yuan, Siyuan Liu, Jiawei Zhang, Yongbing Zhang, Chao Dong, and Liang Lin. Un-supervised image super-resolution using cycle-in-cycle generative adversarial networks. In *Proceedings of the IEEE Conference on Computer Vision and Pattern Recognition Workshops (CVPRW)*, pages 701–710, 2018.
- [45] Xiaozhong Ji, Yun Cao, Ying Tai, Chengjie Wang, Jilin Li, and Feiyue Huang. Real-world super-resolution via kernel estimation and noise injection. In *Proceedings of the IEEE/CVF Conference on Computer Vision and Pattern Recognition Workshops (CVPRW)*, pages 466–467, 2020.
- [46] Shunta Maeda. Unpaired image super-resolution using pseudo-supervision. In *Proceedings of the IEEE/CVF Conference on Computer Vision and Pattern Recognition (CVPR)*, pages 291–300, 2020.

- [47] Jianwen Xie, Ruiqi Gao, Zilong Zheng, Song-Chun Zhu, and Ying Nian Wu. Learning dynamic generator model by alternating back-propagation through time. In *Proceedings of the AAAI Conference on Artificial Intelligence (AAAI)*, volume 33, pages 5498–5507, 2019.
- [48] Jianwen Xie, Ruiqi Gao, Zilong Zheng, Song-Chun Zhu, and Ying Nian Wu. Motion-based generator model: Unsupervised disentanglement of appearance, trackable and intrackable motions in dynamic patterns. In *Proceedings of the AAAI Conference on Artificial Intelligence (AAAI)*, volume 34, pages 12442–12451, 2020.
- [49] Arthur P Dempster, Nan M Laird, and Donald B Rubin. Maximum likelihood from incomplete data via the em algorithm. *Journal of the Royal Statistical Society: Series B (Methodological)*, 39(1):1–22, 1977.
- [50] Max Welling and Yee W Teh. Bayesian learning via stochastic gradient langevin dynamics. In *Proceedings of the International Conference on Machine Learning (ICML)*, pages 681–688. Citeseer, 2011.
- [51] David E Rumelhart, Geoffrey E Hinton, and Ronald J Williams. Learning representations by back-propagating errors. *Nature*, 323(6088):533–536, 1986.
- [52] Diederik P. Kingma and Jimmy Lei Ba. Adam: A method for stochastic optimization. In *Proceedings of the International Conference on Learning Representations (ICLR)*, 2015.
- [53] Jia-Bin Huang, Abhishek Singh, and Narendra Ahuja. Single image super-resolution from transformed self-exemplars. In *Proceedings of the IEEE Conference on Computer Vision and Pattern Recognition*, pages 5197–5206, 2015.
- [54] Roman Zeyde, Michael Elad, and Matan Protter. On single image scale-up using sparse-representations. In *Proceedings on International Conference on Curves and Surfaces*, pages 711–730. Springer, 2010.
- [55] Pablo Arbelaez, Michael Maire, Charless Fowlkes, and Jitendra Malik. Contour detection and hierarchical image segmentation. *IEEE Transactions on Pattern Analysis and Machine Intelligence*, 33(5):898–916, 2010.
- [56] Tim Brooks, Ben Mildenhall, Tianfan Xue, Jiawen Chen, Dillon Sharlet, and Jonathan T Barron. Unprocessing images for learned raw denoising. In *Proceedings of the IEEE/CVF Conference on Computer Vision and Pattern Recognition (CVPR)*, pages 11036–11045, 2019.
- [57] Zhou Wang, Alan C Bovik, Hamid R Sheikh, and Eero P Simoncelli. Image quality assessment: from error visibility to structural similarity. *IEEE Transactions on Image Processing (TIP)*, 13(4):600–612, 2004.
- [58] Andrey Ignatov, Nikolay Kobyshev, Radu Timofte, Kenneth Vanhoey, and Luc Van Gool. Dslr-quality photos on mobile devices with deep convolutional networks. In *Proceedings of the IEEE International Conference on Computer Vision (ICCV)*, pages 3277–3285, 2017.
- [59] David Martin, Charless Fowlkes, Doron Tal, and Jitendra Malik. A database of human segmented natural images and its application to evaluating segmentation algorithms and measuring ecological statistics. In *Proceedings Eighth IEEE International Conference on Computer Vision (ICCV)*, volume 2, pages 416–423. IEEE, 2001.
- [60] Yusuke Matsui, Kota Ito, Yuji Aramaki, Azuma Fujimoto, Toru Ogawa, Toshihiko Yamasaki, and Kiyoharu Aizawa. Sketch-based manga retrieval using manga109 dataset. *Multimedia Tools and Applications*, 76(20):21811–21838, 2017.
- [61] Kai Zhang, Wangmeng Zuo, and Lei Zhang. Ffdnet: Toward a fast and flexible solution for cnn-based image denoising. *IEEE Transactions on Image Processing (TIP)*, 27(9):4608–4622, 2018.

Table 3: Performances of the proposed USRCN method with different ρ values under the degradations combined with scale factor 4, camera sensor noise (Case 3) and 6 different blur kernels on Set14.

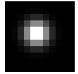
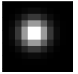

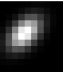
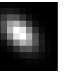
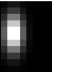


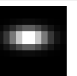

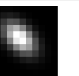

ρ	Blur Kernels						Average
							
0	22.25/0.555	22.60/0.563	23.38/0.563	23.56/0.567	23.80/0.572	23.49/0.566	23.18/0.564
0.01	22.70/0.584	22.99/0.588	23.67/0.585	23.90/0.589	24.05/0.592	23.67/0.582	23.50/0.587
0.10	24.04/0.651	24.35/0.654	24.56/0.638	24.67/0.635	24.72/0.637	24.56/0.636	24.48/0.642
0.20	24.52/0.666	24.72/0.666	24.79/0.649	24.85/0.647	24.85/0.646	24.76/0.648	24.75/0.654
0.30	24.74/0.650	24.59/0.653	24.70/0.646	24.81/0.644	24.84/0.646	24.73/0.645	24.74/0.647
0.40	23.86/0.616	24.04/0.622	24.52/0.633	24.58/0.632	24.64/0.637	24.48/0.631	24.35/0.629
0.50	23.10/0.587	23.34/0.594	24.00/0.611	24.12/0.613	24.27/0.619	23.94/0.610	23.80/0.606



Figure 6: The super-resolving results of the proposed USRCN method under different ρ values with scale factor 3 on one typical real example.





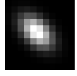
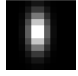
Table 4: Performances of the proposed USRCN method with different γ values under the degradations combined with scale factor 4, camera sensor noise (Case 3) and 6 different blur kernels on Set14.

γ	Blur Kernels						Average
							
0.50	23.74/0.614	23.93/0.620	24.49/0.631	24.52/0.630	24.64/0.636	24.39/0.624	24.29/0.626
0.67	24.52/0.666	24.72/0.666	24.79/0.649	24.85/0.647	24.85/0.646	24.76/0.648	24.75/0.654
0.80	24.52/0.663	24.76/0.663	24.72/0.643	24.80/0.644	24.82/0.642	24.76/0.646	24.73/0.650
1.00	24.38/0.654	24.54/0.655	24.50/0.636	24.62/0.634	24.63/0.635	24.58/0.635	24.54/0.642
2.00	23.35/0.600	23.62/0.605	23.88/0.591	24.02/0.592	24.11/0.596	23.87/0.589	23.81/0.596

B.2 More results

In Table 5, we list the performance comparisons of different methods on the data set CBSD68 [55]. It can be easily observed that the comparison results are very similar with that on Set14 in Table 2, the proposed USRCN method illustrates obvious superiorities than the current state of the art method. Further more, we display more visual results of different methods in Fig. 7 (Gaussian noise), Fig. 8 (spatially variant noise), Fig. 9 (camera sensor noise) and Fig. 10 (real case).

Table 5: PSNR/SSIM results of the compared methods under different degraded combinations on CBSD68. The best results are highlighted in **bold**. The gray results indicate unfair comparison due to mismatched degradations.

Noise types	Methods	Scale factors	Blur Kernels					
								
Case 1	RCAN [34]	×2	25.35 / 0.679	25.33 / 0.671	25.13 / 0.661	24.95 / 0.641	25.40 / 0.672	25.11 / 0.657
	SelfExSR [53]	×2	25.37 / 0.680	25.35 / 0.672	25.17 / 0.663	24.98 / 0.643	25.42 / 0.673	25.15 / 0.659
	ZSSR [1]	×2	24.94 / 0.692	25.04 / 0.697	25.06 / 0.690	24.83 / 0.674	25.44 / 0.709	25.08 / 0.689
	DoubleDIP [21]	×2	24.47 / 0.643	24.67 / 0.650	24.40 / 0.632	25.07 / 0.660	25.10 / 0.665	24.29 / 0.620
	DIPFKP [4]	×2	27.21 / 0.740	26.92 / 0.726	26.56 / 0.720	26.45 / 0.707	26.49 / 0.706	26.49 / 0.714
	USRCN	×2	28.47 / 0.790	28.12 / 0.773	27.74 / 0.769	27.43 / 0.746	27.44 / 0.749	27.56 / 0.757
	RCAN [34]	×3	22.21 / 0.528	22.50 / 0.539	22.76 / 0.545	22.75 / 0.531	23.29 / 0.578	22.82 / 0.547
	SelfExSR [53]	×3	22.44 / 0.538	22.65 / 0.545	22.89 / 0.550	22.86 / 0.537	23.36 / 0.580	22.95 / 0.552
	ZSSR [1]	×3	22.68 / 0.570	22.71 / 0.571	22.80 / 0.570	22.66 / 0.557	23.10 / 0.592	22.96 / 0.580
	DoubleDIP [21]	×3	20.56 / 0.456	20.81 / 0.466	21.36 / 0.482	21.70 / 0.500	21.96 / 0.519	21.28 / 0.483
	DIPFKP [4]	×3	26.53 / 0.711	26.43 / 0.703	25.78 / 0.675	25.49 / 0.660	25.67 / 0.664	25.66 / 0.666
	USRCN	×3	27.34 / 0.758	27.41 / 0.752	26.55 / 0.715	26.47 / 0.703	26.51 / 0.704	26.51 / 0.708
	RCAN [34]	×4	20.14 / 0.446	20.46 / 0.455	21.27 / 0.482	21.33 / 0.473	21.80 / 0.516	21.36 / 0.487
	SelfExSR [53]	×4	20.73 / 0.464	20.94 / 0.473	21.54 / 0.494	21.57 / 0.486	22.01 / 0.524	21.64 / 0.498
	ZSSR [1]	×4	20.67 / 0.474	20.68 / 0.474	20.89 / 0.483	20.64 / 0.464	21.12 / 0.503	20.90 / 0.485
	DoubleDIP [21]	×4	17.91 / 0.349	18.56 / 0.373	19.72 / 0.412	20.04 / 0.425	20.26 / 0.438	19.76 / 0.422
	DIPFKP [4]	×4	25.33 / 0.667	25.44 / 0.667	24.78 / 0.638	24.62 / 0.628	24.72 / 0.630	24.75 / 0.632
	USRCN	×4	25.79 / 0.694	26.10 / 0.699	25.80 / 0.672	25.84 / 0.666	25.89 / 0.668	25.79 / 0.669
Case 2	RCAN [34]	×2	25.07 / 0.640	25.04 / 0.632	24.85 / 0.620	24.69 / 0.603	25.11 / 0.632	24.82 / 0.617
	SelfExSR [53]	×2	25.48 / 0.699	25.46 / 0.691	25.27 / 0.681	25.08 / 0.661	25.53 / 0.691	25.25 / 0.677
	ZSSR [1]	×2	25.00 / 0.690	25.08 / 0.688	25.05 / 0.681	24.88 / 0.668	25.35 / 0.694	25.07 / 0.680
	DoubleDIP [21]	×2	24.33 / 0.628	24.54 / 0.635	24.31 / 0.619	24.86 / 0.644	24.67 / 0.642	24.14 / 0.608
	DIPFKP [4]	×2	27.04 / 0.734	26.88 / 0.722	26.56 / 0.715	26.36 / 0.701	26.36 / 0.701	26.50 / 0.707
	USRCN	×2	27.86 / 0.767	27.59 / 0.753	27.31 / 0.748	27.03 / 0.729	27.07 / 0.731	27.16 / 0.738
	RCAN [34]	×3	22.10 / 0.505	22.38 / 0.514	22.63 / 0.5189	22.62 / 0.506	23.13 / 0.550	22.69 / 0.521
	SelfExSR [53]	×3	22.49 / 0.551	22.71 / 0.559	22.95 / 0.564	22.91 / 0.551	23.43 / 0.595	23.01 / 0.567
	ZSSR [1]	×3	22.73 / 0.567	22.77 / 0.569	22.83 / 0.567	22.73 / 0.557	23.12 / 0.585	23.00 / 0.576
	DoubleDIP [21]	×3	20.30 / 0.429	20.68 / 0.444	21.12 / 0.457	21.49 / 0.478	21.69 / 0.492	21.20 / 0.464
	DIPFKP [4]	×3	26.40 / 0.702	26.37 / 0.692	25.69 / 0.664	25.45 / 0.650	25.57 / 0.654	25.52 / 0.656
	USRCN	×3	26.97 / 0.731	27.02 / 0.728	26.26 / 0.697	26.14 / 0.685	26.25 / 0.688	26.22 / 0.691
	RCAN [34]	×4	20.09 / 0.429	20.39 / 0.438	21.18 / 0.463	21.23 / 0.455	21.69 / 0.495	21.26 / 0.467
	SelfExSR [53]	×4	20.76 / 0.474	20.98 / 0.483	21.58 / 0.505	21.61 / 0.497	22.06 / 0.535	21.68 / 0.510
	ZSSR [1]	×4	20.71 / 0.473	20.73 / 0.473	20.94 / 0.483	20.74 / 0.467	21.18 / 0.500	20.96 / 0.484
	DoubleDIP [21]	×4	17.80 / 0.325	18.12 / 0.334	19.45 / 0.377	19.78 / 0.397	19.97 / 0.397	19.61 / 0.392
	DIPFKP [4]	×4	25.15 / 0.651	25.30 / 0.651	24.68 / 0.621	24.56 / 0.611	24.60 / 0.615	24.59 / 0.616
	USRCN	×4	25.45 / 0.669	25.75 / 0.677	25.47 / 0.652	25.47 / 0.645	25.54 / 0.648	25.44 / 0.647
Case 3	RCAN [34]	×2	24.98 / 0.648	25.00 / 0.642	24.86 / 0.634	24.73 / 0.618	25.09 / 0.641	24.85 / 0.631
	SelfExSR [53]	×2	24.97 / 0.647	24.99 / 0.641	24.86 / 0.633	24.72 / 0.617	25.08 / 0.640	24.84 / 0.630
	ZSSR [1]	×2	24.98 / 0.683	25.02 / 0.680	25.00 / 0.674	24.84 / 0.662	25.24 / 0.683	25.01 / 0.673
	DoubleDIP [21]	×2	23.76 / 0.597	23.86 / 0.599	23.67 / 0.580	24.20 / 0.605	24.09 / 0.605	23.93 / 0.593
	DIPFKP [4]	×2	26.69 / 0.720	26.55 / 0.710	26.29 / 0.702	26.20 / 0.690	26.27 / 0.692	26.12 / 0.695
	USRCN	×2	27.35 / 0.754	27.20 / 0.743	26.99 / 0.736	26.84 / 0.724	26.84 / 0.724	26.85 / 0.729
	RCAN [34]	×3	22.17 / 0.520	22.36 / 0.526	22.61 / 0.529	22.60 / 0.519	23.00 / 0.550	22.66 / 0.530
	SelfExSR [53]	×3	22.29 / 0.523	22.45 / 0.528	22.68 / 0.531	22.66 / 0.521	23.05 / 0.551	22.74 / 0.532
	ZSSR [21]	×3	22.81 / 0.569	22.84 / 0.570	22.87 / 0.567	22.79 / 0.560	23.10 / 0.580	22.98 / 0.572
	DoubleDIP [1]	×3	20.47 / 0.437	20.62 / 0.446	20.74 / 0.437	21.11 / 0.451	21.14 / 0.459	20.78 / 0.440
	DIPFKP [4]	×3	25.44 / 0.660	25.46 / 0.654	25.18 / 0.634	25.05 / 0.626	25.01 / 0.624	25.07 / 0.627
	USRCN	×3	25.93 / 0.697	25.97 / 0.692	25.66 / 0.669	25.59 / 0.661	25.62 / 0.661	25.61 / 0.664
	RCAN [34]	×4	20.46 / 0.450	20.63 / 0.456	21.18 / 0.473	21.22 / 0.468	21.57 / 0.494	21.25 / 0.476
	SelfExSR [53]	×4	20.75 / 0.460	20.90 / 0.465	21.39 / 0.480	21.41 / 0.475	21.75 / 0.500	21.46 / 0.483
	ZSSR [1]	×4	20.88 / 0.487	20.90 / 0.486	21.05 / 0.491	20.92 / 0.484	21.24 / 0.504	21.05 / 0.493
	DoubleDIP [21]	×4	18.23 / 0.344	18.50 / 0.353	19.27 / 0.371	19.40 / 0.375	19.67 / 0.387	19.42 / 0.380
	DIPFKP [4]	×4	24.30 / 0.607	24.33 / 0.605	24.09 / 0.586	24.07 / 0.580	24.08 / 0.581	24.06 / 0.581
	USRCN	×4	24.66 / 0.640	24.75 / 0.640	24.69 / 0.623	24.72 / 0.618	24.74 / 0.619	24.67 / 0.619

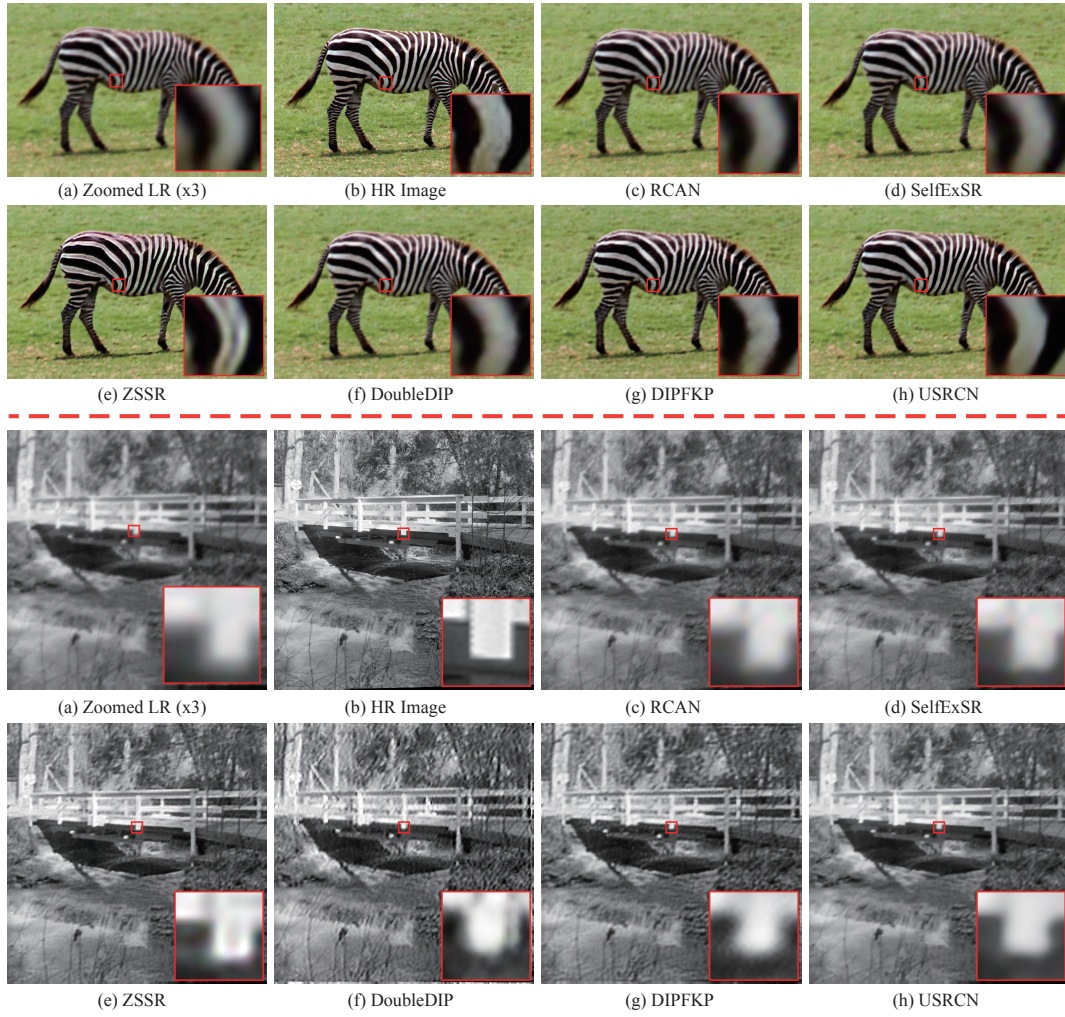


Figure 7: Visual super-resolved results of different methods for the degradations under the Gaussian noise (Case 1) with scale factor 3.

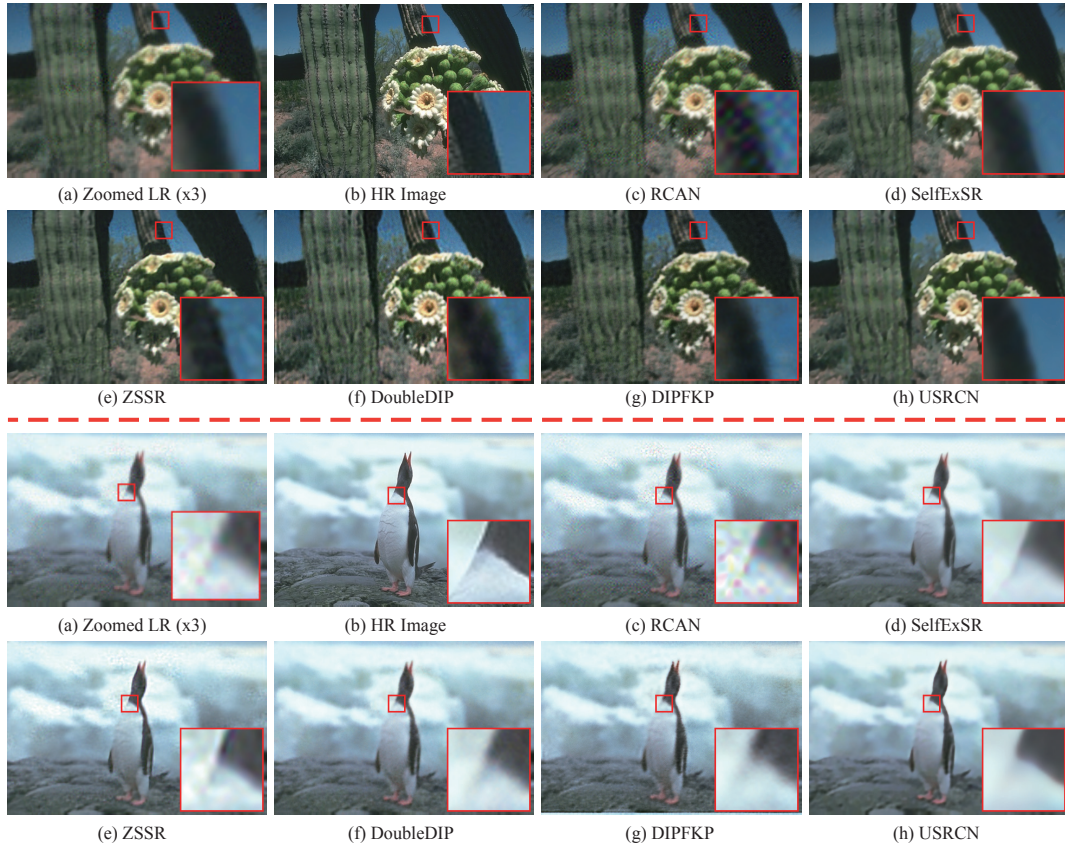


Figure 8: Visual super-resolved results of different methods for the degradations under the spatially variant noise (Case 2) with scale factor 3.

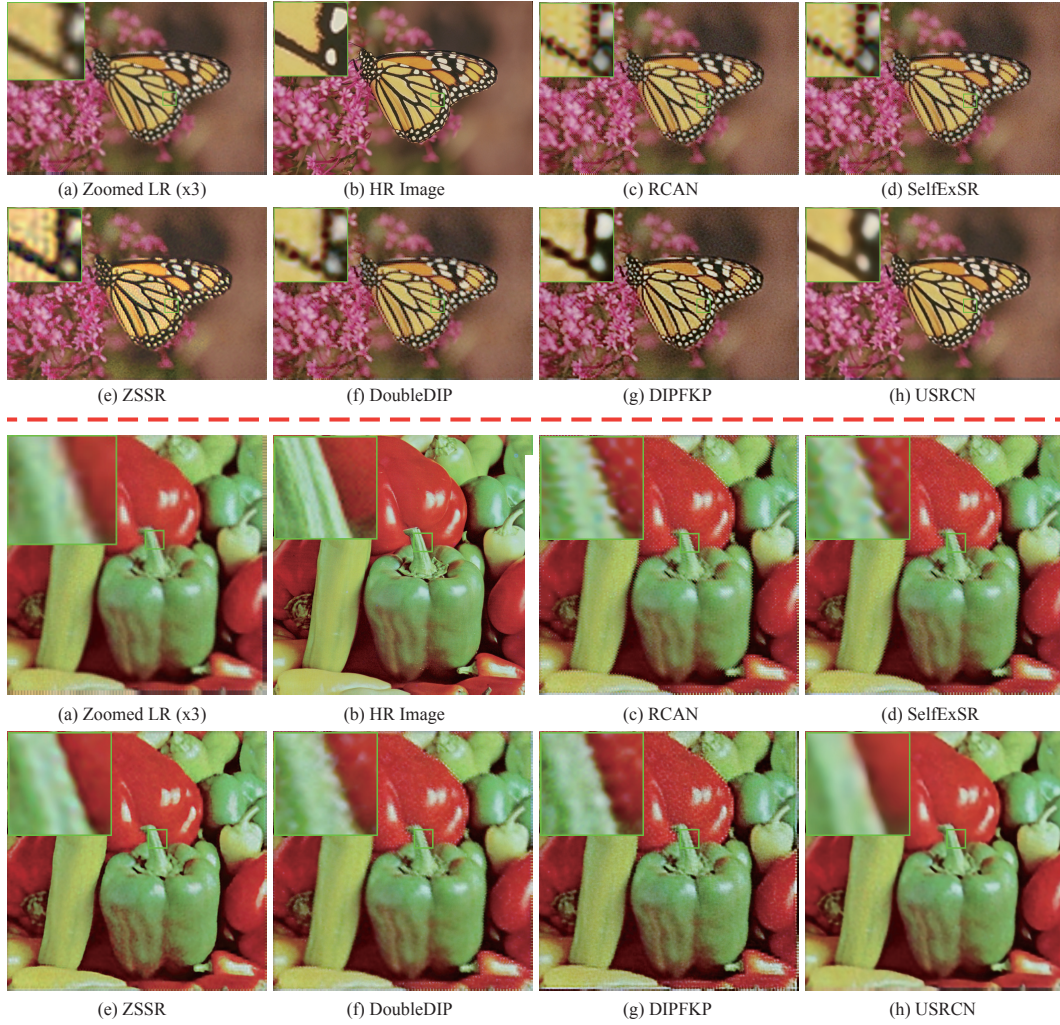


Figure 9: Visual super-resolved results of different methods for the degradations under the camera sensor noise (Case 3) with scale factor 3.



Figure 10: Visual super-resolved results of different methods on two typical real examples in RealSRSet [43] with scale factor 3.